Bidirectional Reflectance Distribution Function Modeling Considerations in Small Unmanned Multispectral Systems

Robert L. Fischer , William J. Shuart, John E. Anderson, Richard D. Massaro , *Member, IEEE*, and Jeffrey G. Ruby

Abstract—With the rapid advancement of miniaturized sensors and unmanned airborne system (UAS) platforms, scientific measurements that previously were carried out by large government or academic institution programs can now be successfully accomplished by smaller collection activities. In the case of vegetation assessment (e.g., forestry and agriculture), spatial, temporal, radiometric, and spectral resolution can be rigorously controlled. Although each of these is important, accurate temporal assessment of chemistry and morphological plant attributes is heavily dependent on spectral resolution and correction. A particular phenomenology of interest is the extraction and modeling of bidirectional reflectance distribution function (BRDF) data. In this effort, an approach is discussed to reflectance calibrate and derive BRDF signatures from soybeans through a newly available multispectral sensor integrated to an industry common UAS platform. Methods were developed to extract the reflectance data across the azimuth and elevation observations and fit these field data to previously derived models from the literature. A modular processing pipeline was developed to allow for the implementation of additional algorithms and efficient numerical analysis. Results show that the coefficients derived to fit the modeled BRDF data are consistent across spatial resolution and within cover type. Additionally, the modeled-fit root-mean-square error was inversely proportional to the spatial resolution of the image data used for signature extraction. In conjunction with more traditional spectral and ratio-based analytical indices, this approach provides important dimensionality in both classification and land-cover assessment applications critical to more accurate temporal vegetation assessment.

Index Terms—Crops, multispectral imaging, radiometry, remote sensing, spectroradiometry, vegetation.

I. Introduction

THE ability to extract scientific measurements from a range of systems has been key to the advancement of earth observation. Applying advanced physical, mathematical, and signal processing techniques from other fields was a hallmark of Prof. David Landgrebe's remote sensing contributions [1].

Robert L. Fischer is with the Strategic Alliance Consulting, Inc., Warrenton, VA 20186 USA (e-mail: robert.fischer@strategicaci.com).

William J. Shuart, John E. Anderson, Richard D. Massaro, and Jeffrey G. Ruby are with the US Army Engineer Research and Development Center, Geospatial Research Laboratory-Corbin Field Station, Woodford, VA 22580 USA (e-mail: william.j.shuart@erdc.dren.mil; john.anderson@erdc.dren.mil; ricky.d.massaro@erdc.dren.mil; jeffrey.g.ruby@erdc.dren.mil).

In particular, his advocacy of signature collection, multispectral and hyperspectral processing, and modeling is directly correlated to the understanding and building of software tools that is the focus of this effort [2]–[5].

The interplay of Sun angle, sensor viewing geometry, and topography are major challenges to the collection of robust spectral data from nontraditional platforms such as that acquired by low altitude small unmanned aerial systems (SUAS). These phenomena can introduce variations in the radiance/reflectance data collected from spectral frame cameras. The bidirectional reflectance distribution function (BRDF) describes how electromagnetic radiation is reflected as a function of the geometric structure of the object under view, the illumination source (typically the Sun), and the viewing geometry [6]. The objective of this effort is to develop an approach (e.g., software pipeline) to collect, preprocess, extract, and model BRDF information obtained from SUAS systems. This process will help strengthen and standardize temporal and morphological analysis using SUAD multispectral systems.

Methods to describe and model the BRDF of materials vary between pure empirical approaches that use regression of actual data to trigonometric functions, and methods that are derived from first principles radiation-transfer and scattering physics for the material and geometrical microstructure of the objects under investigation. Example empirically based models include those by Walthall *et al.* [7], Shibayama and Wiegand [8], Latifovic *et al.* [9], and Ranson *et al.* [10]. While these approaches can replicate overall BRDF shape, models that consider specular reflection and hotspots found with leaf surfaces and vegetation canopies have been found to be more representative of spatial and spectral canopy structure [11].

More rigorous and complex approaches that separate the reflectance phenomena into geometric and volumetric components or kernels have been proposed. These models build upon first principle geometric and volumetric scattering theory and introduce coefficients/parameters that allow for application across varying soil, vegetative, and cultural land-cover classes. Examples of well-documented kernel-based models include those by Roujean *et al.* [12], Wanner *et al.* [13], and the Ross-Li model [14], [15].

To support understanding of directional reflectance, particularly with respect to remote sensing applications,

researchers have conducted extensive ground-based collection efforts. These datasets used radiometric sensors collecting data under controlled conditions. Typically, a radiometer would be affixed to a gantry or other structure such as a goniometer, allowing the instrument to observe the same small area from almost the entire azimuth and zenith observation hemisphere. A seminal device developed for this application was the Portable Apparatus for Rapid Acquisition of Bidirectional Observations of the Land and Atmosphere (PARABOLA). The PARABOLA could sample in 15° instantaneous field-of-view (FOV) sectors in three narrow-bandpass spectral channels for the acquisition of radiance data for almost the entire sky- and ground-looking hemispheres in approximately 10 s [16]. This instrumentation was used for multiple large cross-calibration efforts to include the First International Satellite Land Surface Climatology Project (ISLSCP) Field Experiment (FIFE) [17].

While the PARABOLA system provided excellent angular hemispherical resolution, the spectral resolution did not satisfy the requirements to support existing and future airborne and spaceborne hyperspectral sensors. To meet this need, the University of Zurich built the FIeld GOniometer System (FIGOS) to support the acquisition and investigation of hyperspectral BRDF data and effects. The FIGOS sensor nominally covered the spectral range from 300 to 2450 nm in 704 spectral bands [18].

More recent goniometer systems include the Manual Transportable Instrument platform for ground-based Spectro-directional observations (ManTIS). The ManTIS uses a novel cantilever approach whose light weight and suspension design allow for spectral radiometric collection in many terrain environments [19].

Further efforts have considered mounting narrow FOV radiometers to rotary UAS aircraft for the collection of directional reflectance information. Burkart et al. [20] successfully collect BRDF data over agricultural targets using an Ocean Optics spectroradiometer mounted to an octocopter UAS.

Additional goniometer-focused efforts have collected polarization information along with the directional spectral data. Polarization data introduces additional dimensionality that can be used for further feature classification, separation, and discrimination [21]–[25].

Supporting theoretical and ground-based investigations, airborne and spaceborne platforms have extended the study of the directional reflectance phenomena. Some of the earliest work was used to study the BRDF signatures in the bands of the National Oceanic and Atmospheric Administration (NOAA) Advanced Very High Resolution Radiometer (AVHRR) satellites. The large spatial and temporal collection ability of the AVHRR sensors made the understanding of directional effects important for spectral understanding [26].

The airborne Advanced Solid-State Array Spectroradiometer and associated ground instrumentation have been used to support multiple field collection exercises to include ISLSCP and FIFE as well as the Boreal Ecosystem-Atmosphere Study (BOREAS) sites in Canada. The BOREAS data included bidirectional spectral reflectance factors, spectral hemispherical reflectance,

simple ratio, normalized difference vegetation index (NDVI), and other spectral indices [27], [28].

Products derived satellite constellations have been used to estimate surface albedo through BRDF models. The MODerate Resolution Imaging Spectroradiometer (MODIS) on the Terra and Aqua satellites has provided a long-term archive BRDF, Nadir BRDF-Adjusted Reflectance (NBAR) albedo products (MCD43). The products have been used to evaluate surface dynamics [29] and agricultural seasons [30]. The Visible Infrared Imaging Radiometer Suite on the Suomi-National Polar-orbiting Partnership satellite also is used to generate BRDF, NBAR, and albedo products that are comparable to the continuous longer timeline MODIS products [31].

With the advancement of autonomous platforms and the reduction in sensor form-factors, multiple authors have and continue to investigate the impact of BRDF phenomena on high spatial resolution remote sensing applications. In particular, Honkavaara et al. have been very active investigating BRDF assessment and correction from UAS aircraft over many land-cover classes [32]–[34]. While the primary objective of these efforts is often to radiometrically "correct" or "normalize," usually to a nadir orientation [35], some researchers are attempting to exploit the angular information within a classification process itself [25].

Over the last decade, the rapid development and use of small-UAS (sUAS) systems (<50 lb./22.6 kg) and sensor payloads have become increasingly popular for a wide range of scientific disciplines and applications and have proven particularly promising for agricultural and forestry assessment. In particular, sUAS imaging multispectral payloads have been used to evaluate vegetation conditions in near-real time allowing for more rapid mitigation and temporal management strategies to be executed [36]. However, sUAS platform size and sensor stability combined with solar illumination and topographic effects can create a situation whereby spectral band radiometric accuracy tends to be challenging. While spatial geometric issues for sUAS have been largely addressed by robust structure-from-motion processing that take advantage of the large number of overlapping images acquired by an imaging sensor, the important issues related to radiometric effects are less mature. While it is possible to conduct concurrent (or near-concurrent) ground spectral measurement to derive values to drive correction models such as empirical line calibration, this procedure is not practical for all scenarios and mission types [37], [38]. True radiometric processing considers sensor camera geometry, topographic and solar attributes across multispectral image frames of data prior to orthometric correction are important to accurately assess in-field variability and characterize change.

Dunford et al. [39] and Stark et al. [40] describe the main factors driving radiometric concerns during multispectral image acquisition as being: 1) the use of wide FOV imaging equipment that creates an inherent radial variation in viewing angle, 2) the solar motion that creates a nonstatic illumination source, and 3) atmospheric and cloud influencing incoming solar radiation over the mission area of interest (AOI) generating alternating shadows. These factors lead to variation of the digital number
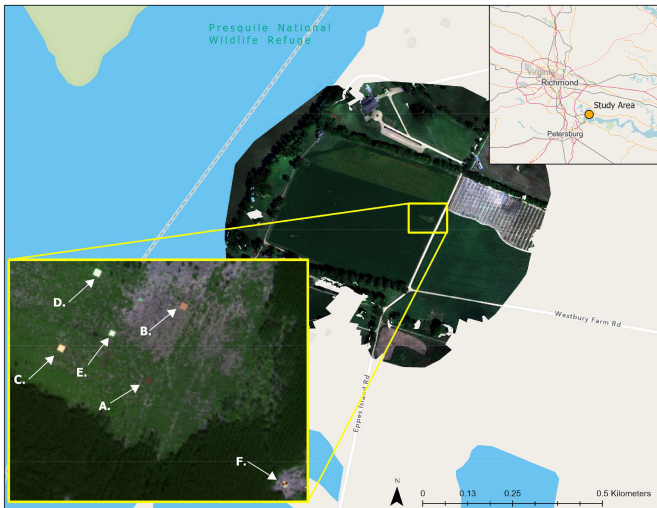
Fig. 1. Location of the Upper Shirley site used in this study. The inset in the upper right shows the location of the site with respect to Richmond, VA, USA. The main figure is the natural color orthomosaic created by Agisoft Metashape overlaid on a Google Maps Street layer. The lower left inset shows the reflectance and geometric calibration panels. The panels are: A = 8%, B = 15%, C = 25%, D = 40%, and H = 99% (Halon Standard). Panel F is an Aeropoint that was used for overall geometric registration/verification.
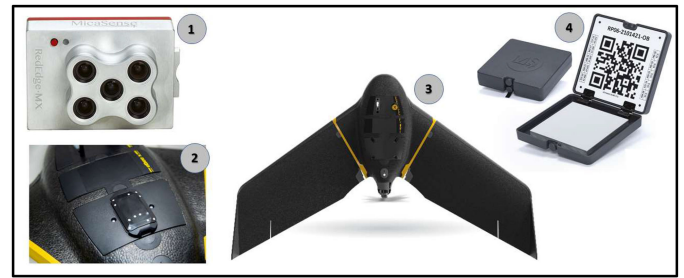

Fig. 2. UAS aircraft and sensors used for this effort. Item 1 is the MicaSense Red-Edge MX camera. Items 2 and 3 are the senseFly eBee. Item 4 is the Spectralon reflectance panel that is used for the radiance to reflectance calibration.

TABLE I
MICASENSE RED-EDGE MX SENSOR SPECIFICATIONS

Parameter	Specification
Weight	231.9 g (includes the DLS 2 and cables)
Dimensions	8.7 cm × 5.9 cm × 4.5 cm
External Power	4.2 V DC−15.8 V DC
Wavelength	Blue (475 nm center, 32 nm bandwidth)
	Green (560 nm center, 27 nm bandwidth)
	Red (668 nm center, 14 nm bandwidth)
	Red Edge (717 nm center, 12 nm bandwidth)
	Near-Infrared (842 nm center, 57 nm bandwidth)
RGB Color	Global shutter, aligned with all bands, 12-b
Output	RAW TIFF
GSD	8 cm per pixel (per band) at 120 m above ground level (AGL)
FOV	47.2° Horizontal FOV

(DN) values for the same features across image frames. To address and exploit this variation, radiometric processing must consider the following.

1) Correction of the vignetting effect (changing of the brightness of an image frame from the center to the edge), dependent on the optics of the sensor.
2) Bidirectional reflectance calculation, dependent on the sun azimuth, surface reflection, topography, and illumination.
3) Atmospheric correction, dependent on atmospheric scattering [41].

The efforts described in this article address the bidirectional reflectance calculation.

II. STUDY AREA AND INSTRUMENTATION

Our evaluation and application of BRDF correction models and workflows was accomplished by the acquisition of middle and late growing season data over soybean fields near the James River in Charles City, VA, USA (see Fig. 1). This is an area of diverse agriculture on the coastal plain of Virginia. This site was selected based upon accessibility and the characteristic homogeneity of vegetative crop cover for the radiometric modeling, and the ability to support long-term temporal studies.

Imagery was collected using the senseFly eBee X sUAS platform (Lausanne, Switzerland) and eMotion flight planning software with the MicaSense Red-Edge MX (AgEagle Aerial Systems, Kansas, USA) payload. The MicaSense Red-Edge MX payload (see Fig. 2) is a five-band multispectral payload specifically designed for sUAS applications.

The specific site used for this study was the Shirley Plantation near Charles City, VA, USA. The plantation and farm are an expansive 3.2 km^2 agricultural area dating to 1614 and is a mixture of small grains and vineyards. Our sampling site

(Latitude/Longitude: 37°20′35″N/77°15′27″W) was a flat, 15.6-hectare soybean field of two varietals: 70% black soybeans in the south and 30% white soybeans on the northern edge. The mission date was September 27, 2021. This period covered the end of the local growing season and the beginning of the senescing period before foliage drop characterized by leaf yellowing of the white soybeans and is referred as the "senescing beans" throughout the article.

The MicaSense MX sensor is a lightweight multispectral sensor designed for agriculture applications and features an 8 cm ground sample distance (GSD) at 122 m, up to 1 capture per second with a 47.2° FOV, for all five bands. senseFly incorporates the MicaSense Red-Edge MX sensor into the eBee X sUAS system. Details on the MicaSense Red-Edge MX sensor are presented in Table I.

The senseFly eMotion version 3.20 flight planning and postprocessing software was used to plan, execute flights, and postprocess the Upper Shirley dataset. The eMotion software also incorporates enhanced GPS data from a local or a virtual reference base station to tag position data in the imagery at collection. The MicaSense Red-Edge MX imagery was collected at approximately 77 m (255 ft) AGL to capture a 5 cm (2.0 in) ground sampling distance pixel. The flights were planned and collected at a 75% image overlap in both horizontal and longitudinal directions.

During the flights, a Topcon's TopNet virtual real-time kinematic GPS service reported a 0.07 m overall relative accuracy

of each photo center during the flights. Additionally, an Emlid Reach RS2 base station was placed on a 2.0 m range pole to collect data for 3.2 h before and after flights. The collected Rinex 2.10 file was submitted to NOAA NGS Online User Positioning Service (OPUS). The resulting point from OPUS along with the GPS observations from the Emlid Reach RS2 Rinex 2.10 file was used in eMotion to additionally postprocess kinematic (PPK) the positions of the images. The resulting PPK processing improved the reported relative spatial accuracy of the geotags to 0.015 m.

Radiometric ground control was established by using five ground targets (area = 0.36 m^2) representing different gray levels and were sized following Wang and Myint [27]. The targets consisted of a series of gray paints (formulas by BEHR, Inc.) that are spectrally constant across the visible to the near infrared (VNIR) region of interest. Reflectance spectra were acquired using an SVC HR-1024i ground radiometer (Spectra Vista, Inc., Poughkeepsie, New York, 350–2400 nm) during the mission times of each sUAS flight. Additional signatures were collected within open areas near the soybean fields and included static targets such as road surfaces and soils. The spectra obtained were used in comparing the extracted imagery signatures from the (BRDF) radiometrically corrected orthophotos to the ground data collected concurrently during each mission. The SVC radiometer was used to collect reflectance data in full sunlight at a distance of 1 m (nadir) above the ground target and reflectance calibration was performed by measuring a Spectralon standard following procedures described by Satterwhite and Henley [42]. The spectral resolution for the SVC instrument is ≤3.3 nm full wave half maximum VNIR region and the nominal FOV of the instrument is 4° allowing a sample diameter of 7 cm to be resolved at a 1 m distance.

III. METHODS

To extract the BRDF information from the MicaSense Red-Edge MX sensor, the research team developed an end-to-end processing pipeline shown in Fig. 3. The pipeline includes components from commercial software, Open-Source utilities, and custom-developed MATLAB code. A modular approach was adapted to ensure that future improvements and modifications could easily be swapped or added to the pipeline. As an example, the team currently uses Agisoft Metashape to perform the bundle adjustment and create the output geospatial products (surface models, orthometric images, and camera exterior orientation). However, the pipeline currently supports output from Pix4D, Correlator 3D, and several open-source photogrammetric solutions for geometric processing, and these software packages can be interchanged as desired. It is important to note that BRDF products generated by Agisoft were only the final camera positions during exposure, the surface model, and the individual spectral band orthometric frames. Orthomosaics were only generated for visual products, not for BRDF data extraction.

Geometric processing of the MicaSense data was conducted using the Agisoft Metashape Professional software, version 1.74. Total of 1035 five-band images from September 27 were imported as separate spectral bands using the position and orientation tags from the EXIF header applied by the senseFly
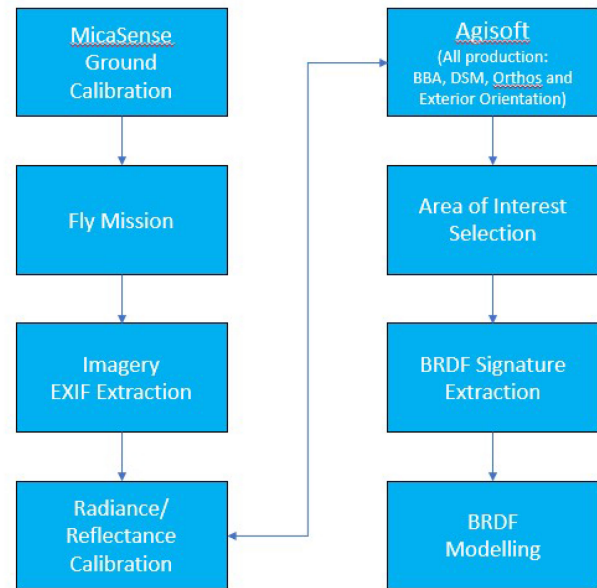

Fig. 3. BRDF modeling pipeline. Each is a modular component that can be improved or replaced as needed.

eMotion software. As a note on nomenclature, we refer to a set of all five spectral bands collected together as an "image" and single spectral bands as "bands" or "frames."

Processing that consisted of image/photo alignment, dense point cloud reconstruction, DEM creation, orthometric image generation, and camera parameter output used the following Metashape settings.
1) Photo Alignment: High.
2) Build Dense Cloud: Medium.
3) Export DEM: Output resolution of 0.20 m (EPSG 32618).
4) Export Orthometric Images: Output resolutions of 0.05–2.0 m (EPSG 32618).
5) Export Camera Parameters: EPSG 32618 – WGS 84/UTM 18, Omega-Phi-Kappa.

Processing was conducted on a Windows 10 Notebook PC (Intel i7 processor, 16 GB of RAM, NVIDIA GeForce RTX 2060 GPU). Processing time from photo ingestion through creation of orthometric images was approximately 1 h. Fig. 4 shows various geometric products created over the study site by Agisoft MetaShape.

The MicaSense manufacturers provide the equipment, metadata, and framework necessary to calibrate the raw DN data to radiance units (in watts per meter squared per steradian). The process consists of the basic following steps [43].
1) Un-bias images by accounting for dark pixel offset.
2) Compensate for imager-level effects (radiometric calibration).
3) Compensate for optical chain effects (vignetting).
4) Normalize images by exposure and gain settings.
5) Convert to common units (radiance).

All values necessary to carry out these calculations are included in customized EXIF tags associated with each image collected (one for each spectral band and exposure position). Customized MATLAB code was developed to read the EXIF information and create radiance versions for each spectral band
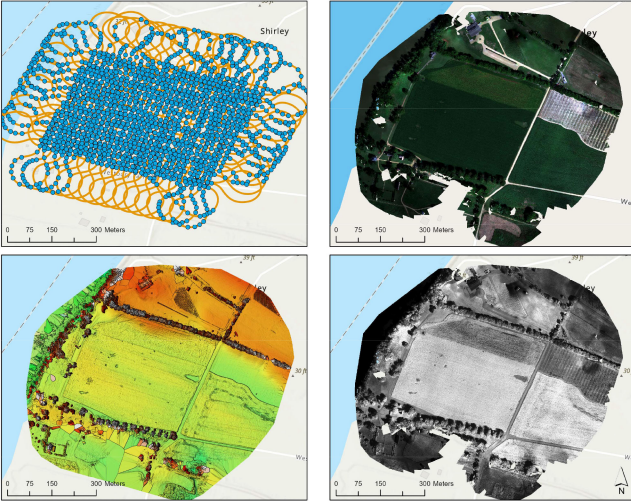
Fig. 4. Geospatial products from the Upper Shirley Soybean fields as created by Agisoft MetaShape. The upper left photograph image shows the flight plan, and the upper right is the RGB orthomosaic. The lower left is the DSM, and the lower right is the NIR orthomosaic.
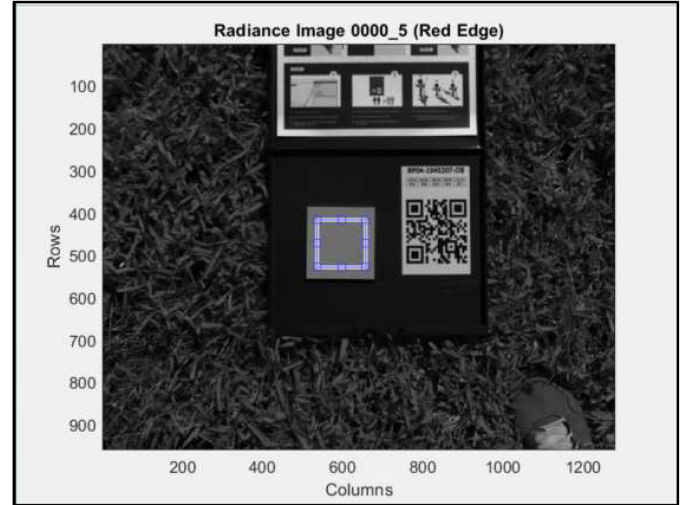

Fig. 5. Sample reflectance calibration image for the MicaSense Red-Edge band (Band 5). The blue box in the center of the frame over the calibration panel shows the pixels that were selected to generate the radiance to reflectance conversion factor.

using the series of equations shown as follows [44]:

$$r = \sqrt{(x - c_x)^2 + (y - c_y)^2} \qquad (1)$$

$$k(x, y) = 1 + k_0 r + k_1 r^2 + k_2 r^3 + \cdots + k_5 r^6 \qquad (2)$$

$$V(x, y) = \frac{1}{k(x, y)} \qquad (3)$$

$$L(x, y) = V(x, y) * \frac{a_1}{g} * \frac{\rho(x, y) - \rho_{bl}(x, y)}{t_e + a_2 - a_3 t_e y} \qquad (4)$$

where

1) x, y are the column and row values from the image;
2) c_x and c_y are the principal point offsets;
3) r is the radial distance;
4) k_n are the radial distortion coefficients;
5) a_n are radiometric calibration coefficients;
6) ρ is the normalized pixel value;
7) ρ_{bl} is the pixel black level value;
8) g is the gain, which is defined as the ISO/100;
9) t_e is the shutter speed in seconds;
10) L is the radiance in (W/m^2/sr).

After creation of the radiance images, reflectance versions can be generated by exploiting ground calibration target images Fig. 5 collected before and/or after each flight as part of the standard MicaSense operations [45]. This panel has previously been reflectance calibrated to NIST standards, and this data has been provided by the manufacturer. Through a simple ratio, a radiance to reflectance conversion factor can be generated for each spectral band and applied to the radiance data generated by the equations provided above. The process described above was conducted for every spectral band of the individual five-band MicaSense images.

It should be noted that while the reflectance/radiance calibration method used above has been the standard approach for the MicaSense Red-Edge camera, MicaSense recently upgraded the
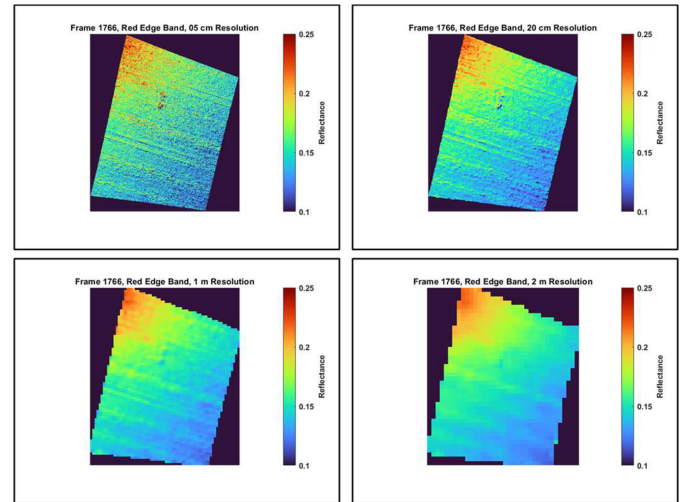
Fig. 6. Single spectral band (the Red-Edge, 717 nm) from an image collected over the Upper Shirley Soybean site after orthorectification. Four different spatial resolutions show the brighter spectral response toward the top-left of the frame (North is up). This corresponds to the backscatter direction where the Sun was in the south-south-east position (about 158°, where 180° is due south).

downwelling radiance sensor [46]. The new downwelling sensor, referred to as the Downwelling Light Sensor 2 (DLS2), employs multiple titled sensors to determine direct and diffuse irradiance components. Usage of a downwelling sensor has been shown to provide reflectance measurements to a broader range of lightning conditions [47]. However, the lack of published cosine response data currently limits the usefulness of the DLS2 [48]. Methods to integrate measurements from this sensor will be added to future versions of the overall processing pipeline shown in Fig. 3 as DLS2 information and calibration data becomes available.

An example of the reflectance calibrated orthometric images is shown in Fig. 6. The figure shows a single spectral band (the Red-Edge, 717 nm) at the four different spatial resolutions

Fig. 7. Shapefiles showing the boundaries within the QGIS software where four of the BRDF signatures were extracted (referred to as AOIs). The four Shapefiles displayed are used throughout the analysis and discussion sections. The base imagery underneath the Shapefiles is the NIR mosaic created via Agisoft Metashape.
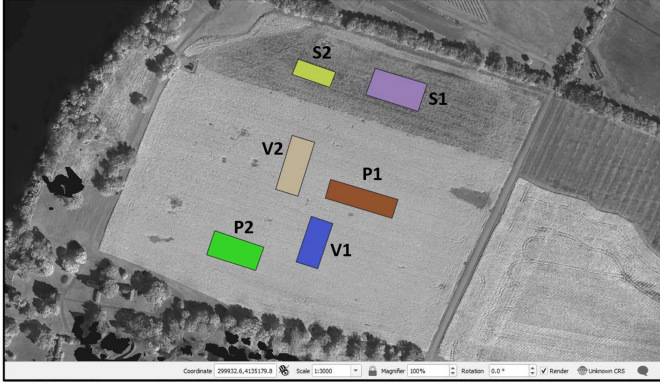
created from Agisoft. As is typically found with vegetation, the soybean canopy generates a strong backscattered signature. This is demonstrated by the higher reflectance toward the top of the frames. This is especially evident at the coarser spatial resolutions, where the row effects are smoothed out via the resampling algorithm used by Agisoft (e.g., the 1 and 2 m examples). Conversely, the denser spatial resolutions pick up the microtopography of the crop row structures, which provides a vertical structure that strongly reflects light back to the sensor, resulting in "noisier" signatures in the 5 and 20 cm examples (top two subfigures in Fig. 6).

After generation of the reflectance calibrated images, multiple AOIs for the test areas were selected based on variation in cover (healthy turgid versus presenescence/yellow) to extract the BRDF signatures. Fig. 7 shows the six of the AOIs that were delineated from the Upper Shirley soybean fields. Of the six AOIs, two were over the healthy, turgid soybeans parallel to the crop rows (noted P1 and P2), two were over the healthy turgid soybeans perpendicular to the crop rows (noted V1 and V2), and two were over the presenescence soybeans (noted S1 and S2). These AOIs were then saved as ArcGIS Shapefiles to be used by the BRDF extraction pipeline. The areas of coverage for these AOIs were as follows.

1) Parallel Soybean 1 (P1): 1900 m^2
2) Parallel Soybean 2 (P2): 1800 m^2
3) Perpendicular Soybean 1 (V1): 1500 m^2
4) Perpendicular Soybean 2 (V2): 1800 m^2
5) Senesced Soybean 1 (S1): 2100 m^2
6) Senesced Soybean 2 (S2): 900 m^2

With the selection of an AOI, the extraction of the BRDF signature can proceed by calculating the intersection between the individual reflectance-calibrated five-band orthometric images generated and the AOI of interest. A series of MATLAB utilities were created to automate this step. A list of the 1035 orthometric images and camera exposure stations were loaded into a MATLAB structure. The code simply loops through these images looking for an intersection between the AOI and orthometric

image boundaries. If an intersection is detected, the ground coordinates of valid pixel (nonzero or background) would be extracted and saved into a second MATLAB structure. Depending upon the size and location of the AOI selected, between 50 and 60 individual frames would intersect with AOI. As the exposure station and solar position of every image is known, it required only a simple geometric transformation to save each pixel value as a function of view zenith, view azimuth, and solar position. A second transformation was employed to convert the view azimuth in earth-centered reference to the solar principal plane reference, which provides the two-dimensional, polar coordinate signatures that are shown in the results throughout the article. The total number of pixels used to generate the polar coordinate signature is dependent upon the resolution of the image source. For the 2 m spatial resolution images, the number of points was roughly 1500 (differed slightly by AOI and spectral band). For the 5 cm images, the number of points was about 2 000 000.

Building upon the observed similarity of BRDF signatures to the limacon equation, Walthall *et al.* proposed a solution where reflectance is a function of the view zenith, view azimuth, the solar azimuth (with respect to the solar principal plane), and a term that represents the nadir reflectance. After extraction of the BRDF signatures and projection into a polar coordinate reference frame, it was a simple matter to empirically fit these signatures to models using the least squares method. This approach is common with the BRDF modeling field (e.g., [49]). Rearranging the terms to improve numerical stability and adding a hotspot correction [50], the modified Walthall equation used was

$$\rho = X1 + X2\theta_i\theta_r\cos\phi + X3\theta_i^2\theta_r^2\left(1 + \frac{1}{\theta_i^2} + \frac{1}{\theta_r^2}\right) + X4D \tag{5}$$

where

$$D = \sqrt{\tan\theta_i^2 + \tan\theta_r^2 - 2*\tan\theta_i\tan\theta_r\cos\phi} \tag{6}$$

and

1) θ_i is the solar zenith angle;
2) θ_r is the viewing zeinth angle;
3) ϕ is the viewing azimuth angle in the solar principal plane.

This yields a series of equations of the form where 1–*n* are the pixel values to be modeled

$$\begin{bmatrix} 1 & \theta_{i1}\theta_{r1}\cos\phi_1 & \theta_{i1}^2\theta_{r1}^2\left(1 + \frac{1}{\theta_{i1}^2} + \frac{1}{\theta_{r1}^2}\right) & D_1 \\ 1 & \theta_{i2}\theta_{r2}\cos\phi_2 & \theta_{i2}^2\theta_{r2}^2\left(1 + \frac{1}{\theta_{i2}^2} + \frac{1}{\theta_{r2}^2}\right) & D_2 \\ 1 & \theta_{i3}\theta_{r3}\cos\phi_3 & \theta_{i3}^2\theta_{r3}^2\left(1 + \frac{1}{\theta_{i3}^2} + \frac{1}{\theta_{r3}^2}\right) & D_3 \\ & & . & \\ & & . & \\ & & . & \\ 1 & \theta_{in}\theta_{rn}\cos\phi_n & \theta_{in}^2\theta_{rn}^2\left(1 + \frac{1}{\theta_{in}^2} + \frac{1}{\theta_{rn}^2}\right) & D_n \end{bmatrix} \begin{bmatrix} X1 \\ X2 \\ X3 \\ X4 \end{bmatrix} = \begin{bmatrix} \rho_1 \\ \rho_2 \\ \rho_3 \\ . \\ . \\ . \\ \rho_n \end{bmatrix} \tag{7}$$

which can be solved via ordinary matrix least squares as

$$\boldsymbol{X} = \left[\boldsymbol{A^T A}\right]^{-1}\boldsymbol{A^T\rho} \tag{8}$$

where *A* is the matrix in (7).

TABLE II
COEFFICIENTS GENERATED FOR THE MODIFIED WALTHALL MODEL FOR THE
UPPER-SHIRLEY SOYBEAN SITES OR AOI

Parallel Soybean 1

Resolution	Band 5 (Red-Edge)					Band 4 (NIR)					Band 3 (Red)					Band 2 (Green)					Band 1 (Blue)				
	X1	X2	X3	X4	RMS	X1	X2	X3	X4	RMS	X1	X2	X3	X4	RMS	X1	X2	X3	X4	RMS	X1	X2	X3	X4	RMS
05 cm	25.17	-7.32	3.90	-10.89	1.39	66.01	3.92	4.44	-12.71	5.85	5.15	1.25	0.57	-1.40	0.30	6.43	1.02	1.25	-2.98	0.75	3.62	-1.08	0.90	-1.89	0.32
20 cm	25.17	-7.52	3.90	-10.89	0.88	65.57	-4.30	4.57	-13.33	3.15	5.06	-1.26	0.57	-1.41	0.11	6.42	1.05	1.25	-2.57	0.27	3.62	-1.98	0.60	-1.89	0.11
1 m	22.72	-6.99	3.84	-10.50	0.28	67.40	-7.04	5.14	-15.72	1.26	3.09	-1.30	0.58	-1.45	0.04	6.92	-1.25	1.31	-2.59	0.13	3.68	-2.03	0.61	-1.63	0.05
2 m	22.57	-6.69	3.79	-10.27	0.21	72.27	-11.12	5.78	-19.66	1.23	3.26	-1.50	0.63	-1.63	0.04	6.93	-1.55	1.36	-2.87	0.11	3.72	-2.09	0.61	-1.99	0.04

Parallel Soybean 2

Resolution	Band 5 (Red-Edge)					Band 4 (NIR)					Band 3 (Red)					Band 2 (Green)					Band 1 (Blue)				
	X1	X2	X3	X4	RMS	X1	X2	X3	X4	RMS	X1	X2	X3	X4	RMS	X1	X2	X3	X4	RMS	X1	X2	X3	X4	RMS
05 cm	24.27	-7.99	3.90	-11.47	1.66	73.97	-12.36	5.80	-20.07	3.89	5.38	-1.60	0.63	-1.73	0.30	7.89	-2.40	1.49	-3.59	0.73	3.72	-2.02	0.58	-1.96	0.32
20 cm	24.59	-8.01	3.85	-11.47	0.76	73.85	-12.23	5.85	-20.02	2.23	5.39	-1.61	0.64	-1.74	0.12	7.75	-2.41	1.52	-3.61	0.32	3.72	-2.01	0.58	-1.95	0.11
1 m	24.21	-8.14	3.84	-11.53	0.34	73.61	-12.01	5.88	-19.83	1.39	3.41	-1.64	0.65	-1.77	0.05	7.77	-2.47	1.52	-3.67	0.16	3.77	-2.15	0.59	-2.00	0.05
2 m	24.12	-7.81	3.81	-11.35	0.28	72.76	-10.75	5.60	-18.85	1.28	3.46	-1.68	0.66	-1.80	0.04	7.31	-2.16	1.47	-3.38	0.14	3.68	-1.95	0.57	-1.91	0.05

Vertical Soybean 1

Resolution	Band 5 (Red-Edge)					Band 4 (NIR)					Band 3 (Red)					Band 2 (Green)					Band 1 (Blue)				
	X1	X2	X3	X4	RMS	X1	X2	X3	X4	RMS	X1	X2	X3	X4	RMS	X1	X2	X3	X4	RMS	X1	X2	X3	X4	RMS
05 cm	22.67	-6.58	3.69	-10.20	1.60	73.82	-12.54	5.62	-20.33	3.85	3.33	-1.31	0.60	-1.47	0.30	7.32	-2.18	1.37	-3.36	0.71	3.60	-1.90	0.58	-1.87	0.11
20 cm	22.82	-6.73	3.67	-10.33	0.72	73.46	-12.54	5.64	-20.03	2.22	3.34	-1.53	0.61	-1.68	0.11	7.49	-2.15	1.40	-3.37	0.28	3.56	-1.80	0.58	-1.94	0.11
1 m	22.90	-6.90	3.62	-10.39	0.33	73.43	-12.50	5.69	-20.03	1.42	3.37	-1.57	0.62	-1.71	0.05	7.50	-2.15	1.39	-3.37	0.15	3.54	-1.82	0.58	-1.81	0.05
2 m	23.45	-7.12	3.66	-10.85	0.20	72.27	-11.67	5.96	-19.08	1.17	3.33	-1.53	0.61	-1.68	0.03	7.53	-2.17	1.30	-3.35	0.11	3.44	-1.72	0.56	-1.72	0.04

Vertical Soybean 2

Resolution	Band 5 (Red-Edge)					Band 4 (NIR)					Band 3 (Red)					Band 2 (Green)					Band 1 (Blue)				
	X1	X2	X3	X4	RMS	X1	X2	X3	X4	RMS	X1	X2	X3	X4	RMS	X1	X2	X3	X4	RMS	X1	X2	X3	X4	RMS
05 cm	23.13	-7.47	3.88	-10.91	1.65	74.71	-14.24	5.80	-21.02	4.15	3.36	-1.63	0.63	-1.74	0.30	7.63	-2.47	1.44	-3.58	0.73	3.69	-2.05	0.61	-1.97	0.32
20 cm	23.20	-7.51	3.87	-10.97	0.76	74.56	-13.80	5.80	-21.59	2.48	3.36	-1.64	0.65	-1.75	0.12	7.64	-2.45	1.44	-3.59	0.29	3.69	-2.03	0.61	-1.97	0.11
1 m	23.21	-7.65	3.85	-10.99	0.33	73.50	-12.79	5.69	-20.80	1.40	3.40	-1.68	0.66	-1.79	0.05	7.68	-2.48	1.45	-3.62	0.15	3.70	-2.06	0.61	-1.98	0.05
2 m	23.02	-7.29	3.88	-10.80	0.26	72.13	-10.48	5.37	-19.15	1.35	3.43	-1.71	0.67	-1.80	0.04	7.71	-2.55	1.45	-3.64	0.15	3.64	-1.97	0.60	-1.92	0.04

Senesced Soybean 1

Resolution	Band 5 (Red-Edge)					Band 4 (NIR)					Band 3 (Red)					Band 2 (Green)					Band 1 (Blue)				
	X1	X2	X3	X4	RMS	X1	X2	X3	X4	RMS	X1	X2	X3	X4	RMS	X1	X2	X3	X4	RMS	X1	X2	X3	X4	RMS
05 cm	27.94	-5.71	5.90	-11.60	4.13	43.37	-6.90	6.13	-14.82	6.41	7.67	1.31	1.49	-3.35	1.24	9.94	-0.41	1.85	-5.41	1.74	4.74	-1.75	0.78	-2.32	0.63
20 cm	27.75	-5.47	5.91	-11.41	2.40	43.17	-6.72	6.15	-14.62	4.59	7.71	1.36	1.50	-3.39	0.70	9.89	-0.37	1.85	-5.37	0.84	4.72	-1.75	0.78	-2.31	0.27
1 m	27.12	-5.09	5.93	-10.98	1.29	44.07	-5.90	6.54	-13.75	2.78	7.88	1.77	1.54	-3.57	0.39	9.80	-0.27	1.84	-5.28	0.40	4.80	-1.85	0.79	-2.39	0.12
2 m	25.37	-2.89	5.71	-9.32	1.02	38.94	-0.59	5.38	-6.08	2.54	8.27	2.11	1.62	-3.61	0.30	9.31	0.15	1.81	-2.93	0.30	4.94	-1.93	0.79	-2.49	0.09

Senesced Soybean 2

Resolution	Band 5 (Red-Edge)					Band 4 (NIR)					Band 3 (Red)					Band 2 (Green)					Band 1 (Blue)				
	X1	X2	X3	X4	RMS	X1	X2	X3	X4	RMS	X1	X2	X3	X4	RMS	X1	X2	X3	X4	RMS	X1	X2	X3	X4	RMS
05 cm	28.43	-7.50	6.59	-13.30	4.24	52.13	-16.08	7.65	-22.96	6.85	7.11	1.08	1.63	-3.00	1.23	10.25	1.27	2.28	-4.24	1.76	4.88	-1.69	0.88	-2.31	0.66
20 cm	28.57	-7.40	6.55	-13.41	2.60	51.78	-15.53	7.54	-22.48	4.85	7.23	1.21	1.66	-3.11	0.74	10.21	1.19	2.26	-4.18	0.90	4.82	1.90	0.89	-2.46	0.30
1 m	29.64	-8.58	6.16	-14.18	1.50	51.39	-15.22	7.52	-22.10	3.16	7.54	1.62	1.70	-3.43	0.40	10.57	1.30	2.20	-4.27	0.46	4.84	-1.96	0.88	-2.52	0.14
2 m	32.97	-10.03	6.03	-15.45	1.05	53.32	-15.05	6.41	-22.42	2.48	7.59	1.61	1.73	-3.39	0.30	10.55	1.32	2.07	-4.38	0.32	4.96	-2.04	0.87	-2.57	0.10

There were four turgid soybean sites (large parallel and vertical) and two senesced sites. X1–X4 correspond to the empirically generated coefficients from the equations above. The rms is the root-mean-squared deviation of the image-derived BRDF data to the modified Walthall model using the coefficients.
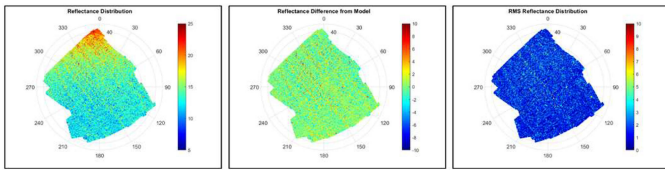

Fig. 8. Red-Edge band from Vertical Soybean AOI 2. Spatial resolution of the imagery was 5 cm. Spatial resolution of the DSM was 20 cm. The left image shows the percent reflectance spatial distribution across the collected view zenith and view azimuth (with respect to the solar principal plane). The center image shows the percent reflectance difference spatial distribution. The right image shows the root-mean-squared percent spatial distribution. Figs. 9–13 have the same left, center, and right graphics, but for different spectral bands and resolutions of the imagery and DSM.
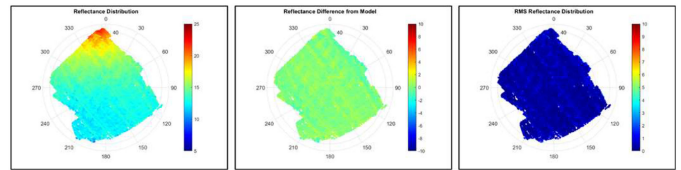

Fig. 9. Red-Edge band from Vertical Soybean AOI 2. Spatial resolution of the imagery was 1 m. Spatial resolution of the DSM was 1 m. A description of the left, center, and right images is provided in the caption of Fig. 8.
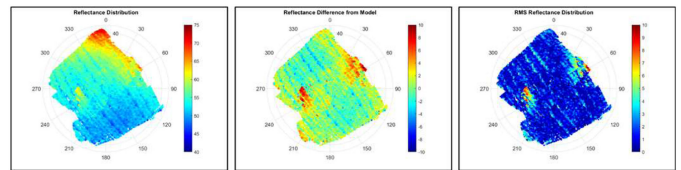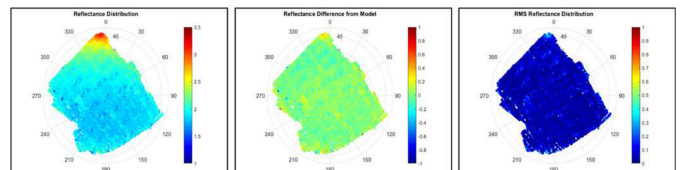

Fig. 10. NIR band from Vertical Soybean AOI 2. Spatial resolution of the imagery was 1 m. Spatial resolution of the DSM was 1 m. A description of the left, center, and right images is provided in the caption of Fig. 8.

Fig. 11. Red band from Vertical Soybean AOI 2. Spatial resolution of the imagery was 1 m. Spatial Resolution of the DSM was 1 m. A description of the left, center, and right images is provided in the caption of Fig. 8.
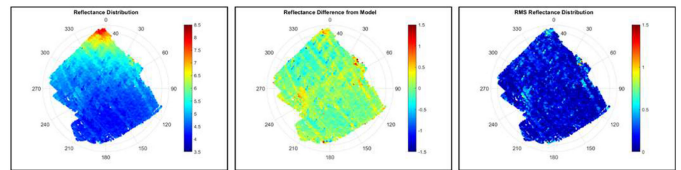

Fig. 12. Green band from Vertical Soybean AOI 2. Spatial resolution of the imagery was 1 m. Spatial resolution of the DSM was 1 m. A description of the left, center, and right images is provided in the caption of Fig. 8.

Equation (8) was solved identically for each spectral band, resolution, and AOI. This produced a series of *X* values for each perturbation as well as corresponding residuals, which are presented in Table II.

The X coefficients and A terms are found to be related to the physical responses. The X1 parameter is the majority of the nadir reflectance value. The X2 term influences the relative forward and backward scattering of the light. A negative value of X2 results in a stronger backscatter signature. The X3 parameter is related to the reflection perpendicular to the solar principal plane. A positive value of X3 will result in a bowl shape. Finally, X4 primarily influences the hotspot correction, but does contribute to the nadir value where both θ_r and ϕ are equal to zero (the polar coordinate origin).

IV. RESULTS AND ANALYSIS

The series of Figs. 8–13 show the results of the BRDF data extracted using the pipeline described above. Each of these figures consists of three subplots. For these figures, we have used percent reflectance (0%–100%) in place of the traditional 0 to 1.0. The plot on the left is the percent reflectance value distribution as a function of view zenith and view azimuth. The center plots show the difference in percent reflectance values between the BRDF data extracted from the imagery and the best fit to the modified Walthall model. The plot on the right shows the root-mean-square (rms) difference between the image-extracted BRDF data and the fit to the modified Walthall model. In all plots, the angular dimension is the view azimuth ($0°$ is the backscatter direction in the solar principal plane), and the radial dimension is the view zenith. The polar position at $0°$, $0°$ would be the nadir reflectance value. Results showed that the SVC signatures of the panels matched the results produced by the pipeline within 2% at a nadir orientation.

The maximum view zenith extracted from this dataset was slightly larger than $45°$. This maximum zenith angle may seem too large given the MicaSense RedEdge MX camera FOV, which has a $28.9°$ maximum radial collection angle. However, the $28.9°$ would only be the limit for a nadir orientation, most of this data
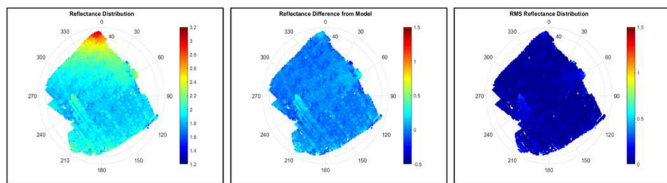
Fig. 13. Blue band from Vertical Soybean AOI 2. Spatial resolution of the imagery was 1 m. Spatial resolution of the DSM was 1 m. A description of the left, center, and right images is provided in the caption of Fig. 8.
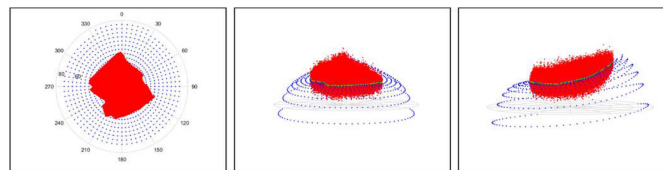

Fig. 14. Red-Edge band from Vertical Soybean AOI 2. Spatial resolution of the imagery was 5 cm. Spatial resolution of the DSM was 20 cm. The left image shows the view zenith and view azimuth spatial distribution of the BRDF data. The center image shows relative reflectance variance from the perspective of the solar principal plane. The right image shows the relative reflectance variance orthogonal to the solar principal plane. Note the right image shows that the BRDF data did not have the zenith range necessary to completely model the hotspot.
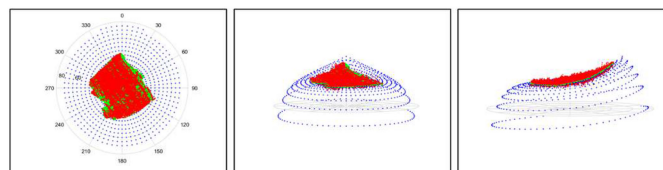

Fig. 15. Red-Edge band from Vertical Soybean AOI 2. Spatial resolution of the imagery was 1 m. Spatial resolution of the DSM was 1 m. A description of the left, center, and right images is provided in the caption of Fig. 14. Note the reduction reflectance variance when compared to Fig. 14.
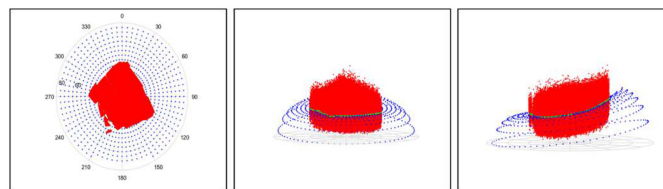

Fig. 16. Red-Edge band from Senesced Soybean AOI 1. Spatial resolution of the imagery was 5 cm. Spatial resolution of the DSM was 20 cm. A description of the left, center, and right images is provided in the caption of Fig. 14.

was collected at pitch angles greater than 10° with roll angles up to 8° (both plus and minus). The largest pitch angle for an image frame that covered the Vertical Soybean AOI 2 was 16.2°, which resulted in maximum zenith angle for some pixels greater than 45°.

Looking at the plots in more detail, Figs. 8 and 9 should be analyzed together. Both figures are derived from the Red-Edge band (center wavelength of 717 nm) from the Vertical Soybean 2 AOI. Fig. 8 was created from the 5 cm spatial resolution orthoimages and the 20 cm spatial resolution surface model. Fig. 9 shows the same band and AOI, but from the downsampled data of 1 m for the orthoimages, and 1 m for the DSM. At a broad level, Figs. 8 and 9 are very similar, the range of the spectral values, difference between the extracted BRDF data and Walthall model, and the rms between the extracted BRDF data and Walthall model are approximately the same. The strong backscatter is shown along the principal plane with the maximum at the largest view zenith (slightly over 45°). Overall, there is no visible spatial bias in reflectance difference and reflectance rms plots, which represents a good fit to the model. What is visible is what can be termed "noise" in the high spatial resolution data. The 5 cm ortho/20 cm DSM dataset has much more "speckle," which is really a function of the spatial nonuniformity of the soybean canopy. At a 5 cm spatial resolution, individual leaves, small spaces/shadows, and vegetation topography are all spatially resolved to some degree, which results in a spectral variability that is evident in the plots. What is also visible is the crop "row" structure of the field. These are the visible lines running from the azimuth angle approximately parallel to the vector that would go from 150°–330°. These crop rows create a canopy topography, which results in a structure where some leaves are oriented more toward the camera, some away (plus shadowing), producing both a bright and dark edge on either side of the row. Even at the coarser spatial resolution, the crop row features are still visible within the data, particularly the reflectance difference data (center plot of Fig. 9).

A second analysis is to review Figs. 9–13. These data show the same plots as previously discussed for the Red-Edge band analysis, but are for the other MicaSense camera spectral bands at orthoimage resolutions of 1 m and DSM resolutions at 1 m. Each of the spectral bands shows the same overall pattern with the strong backscatter in the principal plane and good fit to the modified Walthall model. The worst performing band is the NIR data. Further analysis of Fig. 10 shows some spectral outliers, particularly in the center plot (reflectance difference) and right

plot (rms distribution). In several areas, the BRDF data extracted from the imagery are greater than 10% reflectance more than was predicted by the modified Walthall model (the bright red in these plots). Tracking the source of these data showed that they were from the upper left of the NIR image plane, which likely resulted from an incorrect or out-of-calibration parameter provided via the EXIF header and used within the reflectance calibration step. Verification and/or recalibration will be taking place with the vendor, and the results will be shared in future communications. The reflectance, reflectance difference, and rms distribution plots for the Sensed Soybeans were very similar to the turgid soybeans discussed above.

Another useful analysis is to view the BRDF signature data in a format conducive to understanding the overall structure with the corresponding best fit of the Walthall model. Figs. 14–17 show two sets of data in this format. Here, the left plot for each figure shows a "top-down" view similar to what was presented for Figs. 8–13. The center plot shows a perspective from the solar principal plane from the forward scattering position (180°) to the backscatter position (0°). The right plot shows the data
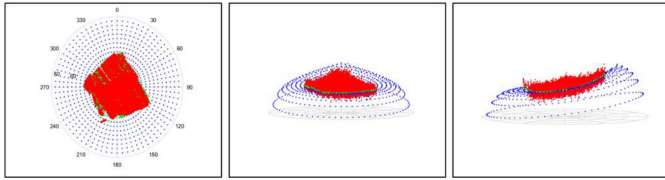
Fig. 17. Red-Edge band from Senesced Soybean AOI 1. Spatial resolution of the imagery was 1 m. Spatial resolution of the DSM was 1 m. A description of the left, center, and right images is provided in the caption of Fig. 14. Note the reduction reflectance variance when compared to Fig. 16.

from a view orthogonal to the solar principal plane. In all plots, the BRDF data extracted from the imagery are red dots, the blue dots are the representative model using the coefficients generated from the best Walthall fit for that set of data, and the green dots are where image-extracted BRDF data would intersect the Walthall surface. What also can be seen in the right images in Figs. 14–17 is that the BRDF data do not have the view zenith range to completely capture the hotspot. With the September 27 collection date and the time of collection, the solar zenith angle was 50°, whereas as noted earlier the maximum view zenith obtained was 45°.

Figs. 14 and 15 show these data for the Red-Edge band from the Vertical Soybean 2 AOI for the 5 cm/20 cm pair and the 1 m/1 m pair. Perhaps the most revealing graphic is the right plot in both these figures that show the data orthogonal to the principal plane. The right plot of the 5 cm/20 cm data (red points) in Fig. 14 shows an overall good fit to the modeled data (in blue) despite the large variance. The right plot of Fig. 15 shows the 1 m/1 m data from the orthogonal view. The overall shape of the 1 m/1 m data matches the 5 cm/ 20 cm in Fig. 14, but has much less variance, so the match to the Walthall model is more easily seen. Also of interest is the center plot from Fig. 15. With the reduced variance in the 1 m/1 m data, it is possible to see the model structure perpendicular to the principal plane in both the extracted and modeled data. Figs. 16 and 17 show the same visual products for the Red-Edge band except for the Senesced Soybean AOI 1. These figures show that the extracted BRDF signatures generally match those collected from goniometer systems like PARABOLOA and FIGOS (e.g., Sandmeier *et al.*) when considering the difference in the plot aspect ratio and vertical exaggeration.

Table II displays the coefficients generated by the pipeline for all the perturbations of the AOIs, ortho and DSM resolution, and spectral band of the MicaSense camera. Two significant digits have been shown for convenience only. A more complete error analysis similar to what is described by Mamaghani and Salvaggio would be necessary to determine the appropriate significant digits and error bounds. This would be a focus of additional communications.

The most obvious and expected pattern that can be seen in Table II is the correlation between spatial resolution of the BRDF extracted data that was modeled and rms difference to the optimal model. As the spatial resolution is reduced (more coarse), the corresponding rms is also reduced. This was visually evident

in the previous figures, especially those showing the orthogonal view of the extracted and modeled data (see Figs. 14–17).

The coefficient values are generally stable with changing resolution and between AOIs of the same cover type. Only a very few coefficients show a sizeable change. The largest was the X2 coefficient for the Senseced Soybean 1 AOI. Here the coefficient changed from –5.90 to –0.09 between the 1 and 2 m resolution runs. The root of this difference has yet to be determined.

V. DISCUSSION

An important aspect of the modular BRDF signature extraction demonstrated is the applicability to other sensors. While this effort focused on the MicaSense Red-Edge camera, any instrument where a per-pixel radiance calibration can be generated should be supported by this pipeline. Even if all required data are not directly provided by the sensor manufacturer, methods to obtain radiance/reflectance calibration can be developed if suitable laboratory instruments are available (e.g., an integrating sphere, spectral radiometers, light meters) [51]. With the ability to obtain radiance units, generating reflectance can proceed using additional calibration information or *in situ* approaches like an empirical line method using field-placed panels or exploiting spectral pseudoinvariant features.

This effort was focused on soybean data in two different phases of the growth cycle on a single day. The collection, processing, and analysis approach used in this study should be easily extendable to other natural and man-made cover types. Understanding the temporal functionality would be beneficial, as the coefficients for the model used could be studied and correlated to physical parameters over time. While only a single model was explored in detail (modified Walthall) to demonstrate the processing pipeline, it would not be a large effort to support any model that is based upon the geometric collection parameters. Although not reported in this document, multiple additional models to include those noted in the introduction have been coded and will be the source of additional communications.

Also of note is that data collected for this effort only extends to a view zenith of approximately 45°. Because of this limited zenith range, the entire hotspot structure was not resolved, only the slope leading to the peak. To generate data with a larger zenith range from a UAS system, a gimbal could be introduced to supplement the wide FOV produced from these short-focal length sensors.

The results from one or more of the BRDF models would be a natural complement to purely spectral indices to include standard measurements such as NDVI and standard vegetation index (SVI). Where NDVI and SVI are traditionally thought of as nadir-based measurements, adding the geometric-based data that generates the BRDF model coefficients would add a depth/dimensionality to a dataset that may allow for the extraction of additional information.

Noting the stablilty of the coefficients generated across the resolutions for the same cover type, there is the potential for this information to be used within a classification or discrimination strategy. While considerably more data collection, analysis, modeling, and verification needs to be conducted, coefficients

related to BRDF model parameters should be usable in this approach. Even with an empirically based approach such as the modified Walthall model, the coefficients are related to the feature canopy and structural components. Models derived from first principal physics and morphology should generate parameter coefficients that are directly related to spectral and geometric traits.

An important next step will be to establish if the MicaSense Red-Edge instrument used for this study provides repeatable radiance measurements via the supplied reflectance calibration parameters. Additional experiments are under design that will place known spectral targets throughout an AOI to verify the stability of the spectral and directional reflectance signatures. These experiments would include additional collections over the Upper Shirley site over a complete growing season. Data collected would not only include the soybean fields reported here but the hay-grass fields and vineyards as well.

Additional sensors and capabilities, particularly those that can be easily integrated to existing sUAS platforms, should be supported by the processing pipeline described in this article. A planned and straightforward addition would be to integrate the MicaSense MX-Blue to the senseFly eBee. This addition would provide ten spectral bands from 444 to 842 nm at bandwidths corresponding to the Sentinel 2 and Landsat 8 satellite systems.

A last and important step would be to rigorously integrate a properly calibrated downwelling irradiance sensor into the processing pipeline. When available, a fully supported and calibrated DLS2 would allow radiance, reflectance, and BRDF measurements to be extracted from the MicaSense sensors across a broader range of atmospheric and lighting conditions. The sensor would provide real-time snapshot of the solar conditions during the exact sensor exposures and would supplement the established reflectance calibration panel approach currently in use.

VI. Conclusion

A miniaturized multispectral sensor mounted on a UAS platform was successfully used to generate BRDF data via a modular processing pipeline. Soybean data represented by two varietals possessing different morphological conditions were collected and processed into reflectance units and fit to an empirical BRDF model. A version of the modified Walthall model was used to fit coefficients across cover type and spatial resolution. Results showed that while the rms fit to the dataset was inversely proportional to the spatial resolution of the image and DSM sources, the model coefficients were stable. This observation is important in both crop and ecological vegetation assessment where data must be normalized (ex. across a growing season) for quick and accurate characterization [52]. In the case of ecological analysis of vegetation, lower resolution data is often more valuable than high-resolution datasets to characterize ecotones and zonation. Since both chemical and morphological components are important diagnostic features of vegetation evaluations, chlorophyll (ex. greenness index) and structural indices such as NDVI would benefit from rigorous radiometric correction procedures that provide the most accurate representation of growing conditions. The interplay of the geometry of the AOI, Sun angle, viewing

orientation, and shadow is best addressed by applying the correction terms afforded by a BRDF workflow in the correction of multispectral UAS imagery.

Our results indicate that BRDF parameter data, in conjunction with more traditional spectral and ratio-based analytical indices, could provide important dimensionality in both classification and land-cover assessment applications critical to more accurate temporal vegetation assessment.

References

[1] D. Landgrebe, *Signal Theory Methods in Multispectral Remote Sensing*. Hoboken, NJ, USA: Wiley, 2003.

[2] D. Landgrebe, "Multispectral land sensing: Where from, where to?," *IEEE Trans. Geosci. Remote Sens.*, vol. 43, no. 3, pp. 414–421, Mar. 2005.

[3] M. Dundar and D. Landgrebe, "Toward an optimal supervised classifier for the analysis of hyperspectral data," *IEEE Trans. Geosci. Remote Sens.*, vol. 42, no. 1, pp. 271–277, Jan. 2004.

[4] V. Madhok and D. Landgrebe, "A process model for remote sensing data analysis," *IEEE Trans. Geosci. Remote Sens.*, vol. 40, no. 3, pp. 680–686, Mar. 2002.

[5] D. Landgrebe, "Introduction to the special issue on analysis of hyperspectral image data," *IEEE Trans. Geosci. Remote Sens.*, vol. 39, no. 7, pp. 1343–1344, Jul. 2001.

[6] F. Nicodemus, "Directional reflectance and emissivity of an opaque surface," *Appl. Opt.*, vol. 4, no. 7, pp. 767–775, 1965.

[7] C. L. Walthall, J. M. Norman, J. M. Welles, G. Campbell, and B. L. Blad, "Simple equation to approximate the bidirectional reflectance from vegetative canopies and bare soil surfaces," *Appl. Opt.*, vol. 24, no. 3, pp. 383–387, 1985.

[8] M. Shibayama and C. L. Wiegand, "View azimuth and zenith, and solar angle effects on wheat canopy reflectance," *Remote Sens. Environ.*, vol. 18, pp. 91–103, 1985.

[9] R. Latifovic, J. Cihlar, and J. Chen, "A comparison of BRDF models for the normalization of satellite optical data to a standard sun-target-sensor geometry," *IEEE Trans. Geosci. Remote Sens.*, vol. 41, no. 8, pp. 1889–1898, Aug. 2003.

[10] K. J. Ranson, J. R. Irons, and C. S. Daughtry, "Surface albedo from bidirectional reflectance," *Remote Sens. Environ.*, vol. 35, no. 2/3, pp. 200–211, 1991.

[11] T. Nilson and A. Kuusk, "A reflectance model for the homogeneous plant canopy and its inversion," *Remote Sens. Environ.*, vol. 27, pp. 157–167, 1989.

[12] J.-L. Roujean, M. Leroy, and P.-Y. Deschamps, "A bidirectional reflectance model of the earth's surface for the correction of remote sensing data," *J. Geophys. Res.*, vol. 97, no. 18, pp. 20455–20468, 1992.

[13] W. Wanner, X. Li, and A. H. Strahler, "On the derivation of kernels for kernel-driven models of bidirectional reflectance," *J. Geophys. Res.*, vol. 100, no. 10, pp. 21077–21089, 1995.

[14] X. Li and A. H. Strahler, "Geometric-optical bidirectional reflectance modeling of a conifer forest canopy," *IEEE Trans. Geosci. Remote Sens.*, vol. GRS-24, no. 6, pp. 906–919, Nov. 1986.

[15] F. Maignan, F.-M. Breon, and R. Lacaze, "Bidirectional reflectance of earth targets: Evaluation of analytical models using a large set of spaceborne measurements with emphasis on the hot spot," *Remote Sens. Environ.*, vol. 90, pp. 210–220, 2004.

[16] D. W. Deering and P. Leone, "A sphere-scanning radiometer for rapid directional measurements of sky and ground radiance," *Remote Sens. Environ.*, vol. 19, no. 1, pp. 1–24, 1986.

[17] D. W. Deering *et al.*, "Prairie grassland bidirectional reflectance measured by different instruments at the FIFE site," *J. Geophys. Res.*, vol. 97, no. D17, pp. 18887–18903, 1992.

[18] S. R. Sandmeier and K. I. Itten, "A field goniometer system (FIGOS) for acquisition of hyperspectral BRDF data," *IEEE Trans. Geosci. Remote Sens.*, vol. 37, no. 2, pp. 978–986, Mar. 1999.

[19] M. Buchhorn, R. Petereit, and B. Heim, "A manual transportable instrument platform for ground-based spectro-directional observations (ManTIS) and the resultant hyperspectral field goniometer system," *Sensors*, vol. 13, pp. 16105–16128, 2013.

[20] A. Burkart, H. Aasen, L. Alonso, G. Menz, G. Bareth, and U. Rascher, "Angular dependency of hyperspectral measurements over wheat characterized by a novel UAV based goniometer," *Remote Sens.*, vol. 7, pp. 725–746, 2015.

[21] T. Berry, C. Morgan, J. Furey, T. DeMoss, J. Kelley, and J. McKenna, "Extensive goniometric spectral measurements at desert sites for military engineering," *Proc. SPIE*, vol. 8495, 2012, Art. no. 84950Z.

[22] T. Berry, E. Lord, and C. Morgan, "Soil polarization data collected for the global undisturbed/disturbed earth (GUIDE) program," *Proc. SPIE*, vol. 9853, 2016, Art. no. 98530R.

[23] J. Furey, S. Zahniser, and C. Morgan, "Laboratory goniometer approach for spectral polarimetric directionality," *Proc. SPIE*, vol. 9853, 2016, Art. no. 98530I.

[24] F.-M. Breon and F. Maignan, "A BRDF-BPDF database for the analysis of earth target reflectances," *Earth Syst. Sci. Data,* vol. 9, pp. 31–45, 2017.

[25] S. Liu, Y. Lin, L. Yan, and B. Yang, "Modeling bidirectional polarization distribution function of land surfaces using machine learning techniques," *Remote Sens.,* vol. 12, pp. 1–21, 2020.

[26] D. S. Kimes, "Dynamics of directional reflectance factor distributions for vegetation canopies," *Appl. Opt.,* vol. 22, no. 9, pp. 1364–1372, 1983.

[27] C. A. Russell, C. L. Walthall, J. R. Irons, and E. C. Brown de Colstoun, "Comparison of airborne and surface spectral bidirectional reflectance factors, spectral hemispherical reflectance and spectral vegetation indices," *J. Geophys. Res.,* vol. 100, no. D12, pp. 25509–25522, 1997.

[28] C. A. Russell, J. R. Irons, and P. W. Dabney, "Bidirectional reflectance of selected BOREAS sites from multiangle airborne data," *J. Geophys. Res.,* vol. 102, no. D24, pp. 29505–29516, 1997.

[29] Z. Wang, C. Schaaf, Q. Sun, Y. Shuai, and M. Roman, "Capturing rapid land surface dynamics with collection V006 MODIS BRDF/NBAR/Albedo (MCD43) products," *Remote Sens. Environ.,* vol. 207, pp. 50–64, 2018.

[30] Z. Wang *et al.*, "Evaluation of MODIS albedo product (MCD43A) over grassland, agriculture, and forest surface types during dormant and snow-covered periods," *Remote Sens. Environ.,* vol. 140, pp. 60–77, 2014.

[31] Y. Liu *et al.*, "Evaluation of the VIIRS BRDF, albedo and NBAR products suite and an assessment of continuity with the long term MODIS record," *Remote Sens. Environ.,* vol. 201, pp. 256–274, 2017.

[32] E. Honkavaara *et al.*, "Remote sensing of 3-D geometry and surface moisture of a peat production area using hyperspectral frame cameras in visible to short-wave infrared spectral ranges onboad a small unmanned airborne vehicle (UAV)," *IEEE Trans. Geosci. Remote Sens.*, vol. 54, no. 9, pp. 5440–5453, Sep. 2016.

[33] E. Honkavaara *et al.*, "Processing and assessment of spectrometric, stereoscopic imagery collected using a lightweight UAV spectral camera for precision agriculture," *Remote Sens.,* vol. 5, pp. 5006–5039, 2013.

[34] T. Hakala *et al.*, "Spectral imaging from UAVs under varying illumination conditions," *Int. Arch. Photogramm., Remote Sens. Spatial Inf. Sci.*, vol. XL-1/W2, pp. 189–194, 2013.

[35] D. Wierzbicki, M. Kedzierski, A. Fryskowska, and J. Jasinski, "Quality assessment of the bidirectional reflectance distribution function for NIR imagery sequences from UAVs," *Remote Sens.,* vol. 10, pp. 1–14, 2018.

[36] S. K. von Bueren, A. Burkart, A. Hueni, U. Rascher, M. P. Tuohy, and I. J. Yule, "Deploying four optical UAV-based sensors over grassland: Challenges and limitations," *Biogeosciences,* vol. 12, no. 1, pp. 163–175, 2015.

[37] C. Wang and S. W. Myint, "A simplified empirical line method of radiometric calibration for small unmanned aircraft systems-based remote sensing," *IEEE J. Sel. Topics Appl. Earth Observ. Remote Sens.,* vol. 8, no. 5, pp. 1876–1885, May 2015.

[38] J. Edwards, J. Anderson, W. Shuart, and J. Woolard, "An evaluation of reflectance calibration methods for UAV spectral imagery," *Photogramm. Eng. Remote Sens.,* vol. 85, pp. 61–70, 2019.

[39] R. Dunford, K. Michel, M. Gagnage, H. Piegay, and M.-L. Tremelo, "Potential and constraints of unmanned aerial vehicle technology for the characterization of Mediterranean riparian forest," *Int. J. Remote Sens.,* vol. 30, no. 19, pp. 4915–4935, 2009.

[40] B. Stark, T. Zhao, and Y. Chen, "An analysis of the effect of the bidirectional reflectance distribution function on remote sensing imagery accuracy from small unmanned aircraft systems," in *Proc. Int. Conf. Unmanned Aircr. Syst.*, Arlington, VA, USA, 2016, pp. 1342–1350.

[41] T. Lillesand, R. Kiefer, and J. Chipman, *Remote Sensing and Image Interpretation*. Hoboken, NJ, USA: Wiley, 2015.

[42] M. B. Satterwhite and J. P. Henley, "Hyperspectral signatures (400 to 2500 nm) of vegetation, minerals, soils, rocks, and cultural features: Laboratory and field measurements," U.S. Army Corps Engineers, Engineer Topographic Lab., Fort Belvoir, VA, USA, Tech. Rep. ELT-0573, 1991.

[43] MicaSense, "MicaSense rededge image processing tutorial 1," Oct. 2021. [Online]. Available: https://micasense.github.io/imageprocessing/MicaSenseImageProcessingTutorial1.html

[44] MicaSense, "RedEdge camera radiometric calibration model," Oct. 7, 2021. [Online]. Available: https://support.micasense.com/hc/en-us/articles/115000351194-RedEdge-Camera-Radiometric-Calibration-Model

[45] MicaSense, "Use of calibrated reflectance panels for rededge data," Oct. 7, 2021. [Online]. Available: https://support.micasense.com/hc/en-us/articles/115000765514-Use-of-Calibrated-Reflectance-Panels-For-RedEdge-Data

[46] MicaSense, "Tutorial 3 - DLS Sensor basic usage," Nov. 7, 2021. [Online]. Available: https://micasense.github.io/imageprocessing/MicaSenseImageProcessingTutorial3.html

[47] K. Schneider-Zapp, M. Cubero-Castan, D. Shi, and C. Strecha, "A new method to determine multi-angular reflectance factor from lightweight multispectral cameras with sky sensor in a target-less workflow applicable to UAVs," *Remote Sens. Environ.*, vol. 229, pp. 60–68, 2019.

[48] J. Suomalainen *et al.*, "Direct reflectance transformation methodology for drone-based hyperspectral imaging," *Remote Sens. Environ.,* vol. 266, pp. 1–19, 2021.

[49] W. Jia, Y. Pang, R. Tortini, D. Schlapfer, Z. Li, and J.-L. Roujean, "A kernel-driven BRDF approach to correct airborne hyperspectral imagery over forested areas with rugged topography," *Remote Sens.,* vol. 12, no. 3, 2020, Art. no. 432.

[50] U. Beisl and N. Woodhouse, "Correction of atmospheric and bidirectional effects in multispectral ADS40 images for mapping purposes," in *Proc. 20th Congr. ISPRS*, Istanbul, Turkey, 2004, pp. 12–23.

[51] B. Mamaghani and C. Salvaggio, "Multispectral sensor calibration and characterization for sUAS remote sensing," *Sensors,* vol. 19, no. 20, 2019, Art. no. 4453.

[52] J. Anderson, R. Fischer, and S. DeLoach, "Remote sensing and precision agriculture: Ready for harvest or still maturing?," *Photogramm. Eng. Remote Sens.,* vol. 65, pp. 1118–1123, 1999.

Robert L. Fischer received the B.S. degree in physics from the Rochester Institute of Technology, Rochester, NY, USA, in 1989, and the Ph.D. degree in computational space sciences from George Mason University, Fairfax, VA, USA, in 2002.

He is currently a Senior Scientist with Strategic Alliance Consulting, Inc., Warrenton, VA, USA. From 1989 to 2021, he served in various roles at the US Army Corps of Engineers, SAIC, and Parsons Corporation to include Senior Scientist, Division Chief Technology Officer, and Directorate Lead. His last position was the Technical Director for the US Army Corps of Engineers, Geospatial Research Laboratory, Fort Belvoir, VA, USA. His research interests include remote sensing, mapping, photogrammetry, image processing, and spectral databases.

Dr. Fischer was the recipient of numerous awards over his government and private industry career including the 2006 US Army's Greatest Invention for the Buckeye System.

William J. Shuart received the B.S. and M.S. degrees in environmental studies from Virginia Commonwealth University, Richmond, VA, USA, in 1997 and 2001, respectively.

He is currently a Geographer with the Army Corps of Engineers Geospatial Research Laboratory, Corbin Field Station, Woodford, VA, USA, and also holds an Assistant Professorship with Virginia Commonwealth University in Life Sciences at the Rice Rivers Center. His research interests include incorporating technology into the environment, using sUAS for mapping, analysis, and artificial intelligence and cartography.

Shuart authored a chapter in the book *GIS for Science* published by ESRI on GeoAI and several peer reviewed articles incorporating sUAS for monitoring and surveying. He was the recipient of several awards for cartography and geospatial analysis over his career.

John E. Anderson received the B.S. degree in environmental science from Mary Washington College, Fredericksburg, VA, USA, in 1981, and the M.S. and Ph.D. degrees in environmental biology from George Mason University, Fairfax, VA, USA, in 1993 and 1996, respectively.

He has worked for the US Army Corps of Engineers in the topographic sciences for more than 30 years as a Research Biologist and was a Postdoctoral Researcher with the Virginia Institute of Marine Science, Gloucester Point, VA, USA, from 1993 to 1996. His areas of expertise are the remote sensing of biological phenomena and terrain characterization using multispectral and hyperspectral imagery. His current research efforts are directed toward unmanned aerial vehicles for high-resolution remote sensing, spectral characterization of Alaska biomes, GPS-less autonomous navigation, and the maturation of tactical frequency-domain topographic laser scanning.

Dr. Anderson has one patent and numerous journal publications and articles related to spectral sensing in the life sciences including two book sections on hyperspectral characterization of iron oxide-based biofilms for detection of acidic mine drainage.

Jeffrey G. Ruby received the B.S. degree in mechanical engineering from Virginia Polytechnic Institute and State University, Blacksburg, VA, USA, in 1992, and the M.S. degree in computer science from George Mason University, Fairfax, VA, USA, in 1998.

Since 1992, he has been a Research Engineer with the US Army Engineer Research and Development Center, Geospatial Research Laboratory-Corbin Field Station, Woodford, VA, USA. He was the Technical Lead for the US Army Buckeye Program from 2005 to 2015. His research interests include photogrammetry, structure from motion, remote sensing, image processing, and computer vision particularly as they apply to automated registration of geospatial data.

Ruby was the recipient of the U.S. Army ERDC Research and Development Achievement Award, Department of the Army Achievement Medal for Civilian Service, U.S. Army Greatest Inventions Award, and the U.S. Army Topographic Engineering Center Award for Leadership Achievement.

Richard D. Massaro (Member, IEEE) received the B.S. degree in physics from James Madison University, Harrisonburg, VA, USA, in 2001, the M.A. degree in astronomy from Boston University, Boston, MA, USA, in 2004, and the Ph.D. degree in computational sciences from George Mason University, Fairfax, VA, USA, in 2011.

Since 2004, he has been a Physical Scientist with the US Army Corps of Engineers Geospatial Research Lab, Alexandria, VA, USA. From 2013 to 2014, he was a Senior Image Scientist with Exelis, Inc., Herndon, VA, USA. He holds two patents, and he has subject matter expertise in several fields of remote sensing, including structure-from-motion, LIDAR, hyperspectral and multispectral imaging, spectroscopy, and low-light level imaging.

Dr. Massaro was the recipient of the United States Geospatial Intelligence Foundation Military Achievement Award and the MG Harold J. Greene Army Award for Innovation (Individual) for his research, development, and subsequent fielding of Full Motion Video-to-3D Mapping software.